

# Silicon solar cells with interfacial passivation of the highly phosphorus-doped emitter surface by oxygen ion implantation

Rajkumar Sahu, Srikanta Palei, Keunjoo Kim\*

Department of Mechanical Engineering and Research Center of Industrial Technology, Jeonbuk National University, Jeonju, 54896, Republic of Korea



## ARTICLE INFO

**Keywords:**  
 Silicon solar cell  
 Oxygen ion  
 Ion implantation  
 Diffusion  
 Interfacial passivation  
 Defects

## ABSTRACT

We investigated oxygen passivation at the interfacial silicon surface on the highly phosphorus-doped region by oxygen ion implantation and showed resulting enhanced electrical properties of silicon solar cells. The oxygen ion implantation converts the dead layer formed due to crystallographic defects in the doping process into an oxygen-induced insulation layer by fragmentation with an optimal amount of energy. The surface dead layer of the highly doped Si emitter was broken by oxygen ions with a fixed-dose and different energies. The optimized implanted oxygen ion energy shows an improved short circuit current after implantation and improved efficiency with enhanced quantum efficiency in the blue region. On the other hand, high energy implanted oxygen ions formed surface defects, resulting in decreased cell efficiency.

## 1. Introduction

Surface passivation of silicon solar cells was extensively investigated to improve the photovoltaic parameters of solar cells by reducing carrier recombination at the emitter surface [1]. In standard silicon solar cell processes, the diffusion process is used to form an emitter layer. During this process, the initial phosphosilicate glass (PSG) layer is formulated on Si surface for a diffusion channel. The high concentration of phosphorus that exceeds solubility limits forms phosphorous precipitates that function as defects, causing the excess dopant to become electrically inactive; these excess precipitates cause Shockley-Read-Hall recombination [2]. The surface-near emitter bulk layer containing excess phosphorous precipitates causes carrier recombination, so the highly doped emitter region turns into a dead layer [3]. This highly doped dead layer is good for Ohmic contact between the silicon emitter and silicon nitride ( $\text{SiN}_x$ ) antireflection coating layer (ARC). However, special care is needed during the surface passivation to prevent electron-hole recombination due to the large space charge density.

The most common dielectric layers used for surface passivation are hydrogenated silicon nitride ( $\text{SiN}_x\text{-H}$ ) [4], silicon dioxides ( $\text{SiO}_2$ ) [5], combined  $\text{SiO}_x/\text{SiN}_x\text{-H}$  [6], silicon oxynitrides ( $\text{SiON}_x$ ) [7], aluminum oxides ( $\text{Al}_2\text{O}_3$ ) [8], hafnium oxide ( $\text{HfO}_2$ ) [9], gallium oxide ( $\text{Ga}_2\text{O}_3$ ) [10], and titanium oxide ( $\text{TiO}_2$ ) [11]. These passivating layers are deposited through thermal oxidation, anodic oxidation, plasma-enhanced chemical vapor deposition (PECVD), and thermal

atomic-layer deposition (ALD) [12]. The thermally grown interfacial layer provides better insulating properties than deposited thin films. Thermally grown oxides show stable interfacial chemical bonding structures on the Si surface with the minimum dangling bonds at the interface. Despite the advantage of a thermal oxide insulation at the interface, the oxide layer at the Ohmic contact region must be removed to prevent degradation because it is hard for the Ag paste to penetrate into the oxide layer during co-firing in the standard cell process. To address the standard cell process without interrupting the interfacial oxide layer, we consider the removal of the dead layer of the cell by transforming it into  $\text{SiO}_x$  or nanocrystallites by the process of oxygen ion implantation.

In this work, oxygen ion implantation was conducted at various energies of 10, 16, 26, 30, and 50 keV with a dose of  $2 \times 10^{14}/\text{cm}^2$  to create a thin insulation layer at the emitter surface of the Al back-surface field Si solar cells. The implanted cells with low energies of oxygen ions formed thin insulation layers and improved the minority carrier lifetimes compared to the reference and other high-energy oxygen ion-implanted cells. Furthermore, the external quantum efficiency was improved in the blue and ultraviolet spectral regions indicating that the recombination centers at the dead emitter layer are strongly reduced. The improvement in interfacial surface passivation results in an increase in the short-circuit current density, fill factor, and efficiency without using any explicit light-trapping techniques. This signifies the importance of 16 keV low-energy oxygen ion implantation. The solar cells

\* Corresponding author.

E-mail address: [kimk@jbnu.ac.kr](mailto:kimk@jbnu.ac.kr) (K. Kim).

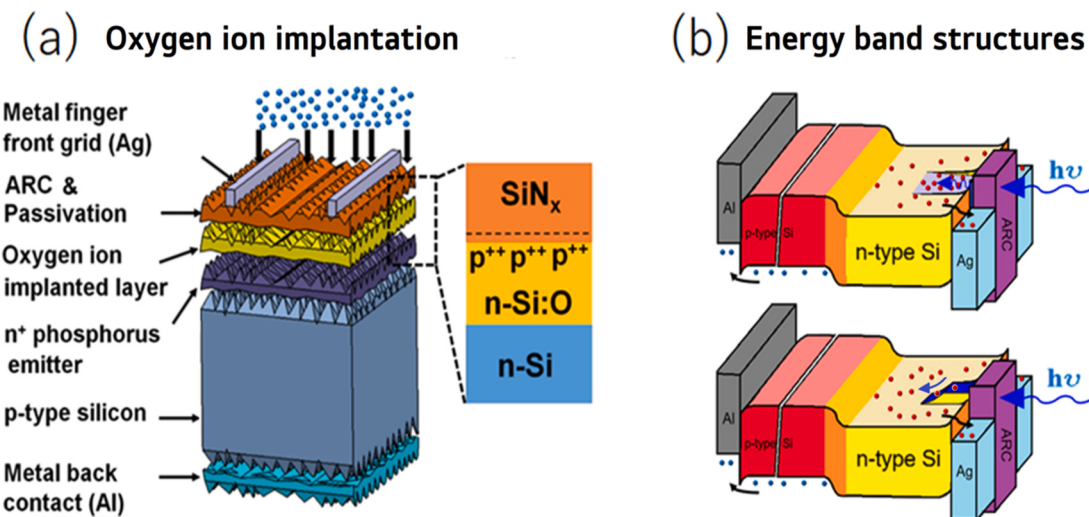


**Fig. 1.** Schematic diagrams of (a) the c-Si solar cell structure with oxygen ion implantation and (b) the corresponding energy band diagram of the solar cell with the formation of Si nanocrystallites near the  $\text{SiN}_x/\text{Si}$  interface by oxygen ion implantation. The implanted interfacial region shows that the bandgap increases with the quantum dot barriers of nanoparticle formation and repels the carriers to move to the electrode even though there is a Schottky barrier in the contact region.

implanted with high-energy oxygen ions showed defects that increased the surface recombination of the minority carriers due to damage by ion implantation and thereby reduced the cell performance.

## 2. Experimental details

Monocrystalline Si solar cells were fabricated with an ultrathin insulation layer on the Si surface with a capping layer in the non-metalized region as shown in Fig. 1 (a). The experiment was performed on p-type boron-doped single-crystalline 6-inch Si (100) wafers with a specific resistivity of 0.3–5  $\Omega\text{-cm}$  and a thickness of  $180 \pm 20 \mu\text{m}$ . At first, we removed the saw damage and conducted wafer cleaning processes. Then, the micro-texturing process was performed to form micro pyramidal structures on wafer surfaces by etching in a KOH-IPA solution at 80 °C for 25 min. The n-type Si emitter layer was formed by the phosphorus oxychloride ( $\text{POCl}_3$ ) doping process in a tube furnace at 920 °C for 10 min. The resulting sheet resistance was about 78.5  $\Omega/\text{sq}$ . The PSG layer formed during the doping process on the Si surface was removed by dipping in a 10% dilute hydrofluoric solution for 30 s, followed by deionized water rinsing and drying processes. An anti-reflection coating layer of 80 nm thick  $\text{SiN}_x$  was deposited by PECVD at 400 °C for 45 s. The metallization process was carried out to form a bus bar and finger lines as a front contact via a screen printing process using Ag paste. A back contact on the rear surface was formed by Al paste and drying at 180 °C and 230 °C for 1.3 min and 45 s, respectively. Finally, the co-firing process was carried out in a temperature range from 622 to 975 °C in a belt-type furnace. Next, laser edge isolation was performed as the last step of the cell fabrication at a laser current of 40 A and a frequency of 50 kHz to enhance the shunt resistance. To form an insulation layer, the fabricated cells were implanted with oxygen ions of various energies of 10, 16, 26, 30, and 50 keV with a dose of  $2 \times 10^{14}/\text{cm}^2$  using a gaseous ion beam implanter. The implantation was carried out on the wafers at a tilt angle of 7° from the <100> direction and a twisted angle of 22.5° from the <110> direction to control the depth of the oxygen ion profile. We analyzed the partial bond orders and valence angles in the implanted structure as shown in Fig. 1(a). We found that all oxygen atoms have a total bond order of 2 to Si atoms, indicating that no radicals remain in the system after implantation. This indicates that there are no Si radicals in the system; the fraction of the Si-Si bonds drops rapidly, whereas that of P-O bond increases. Fig. 1 (b) showed the corresponding energy band diagram before and after the oxygen ion implantation with the formation of the Si nanocrystallites near the  $\text{SiN}_x$ /

Si interface. The implanted interfacial region shows the increased bandgap with the quantum size effect of Si nanodots and repels the carriers to move to the electrode even though there is a Schottky barrier in the contact region.

First, we did simulations to calculate the projected range of oxygen ions using the stopping range of ions in matter (SRIM) simulation code. Various measuring tools were used to characterize the fabricated solar cells. The structural morphologies of oxygen ion-implanted layers were characterized using a field emission scanning electron microscope (FE-SEM) and spherical aberration-corrected transmission electron microscopy (Cs-TEM). The deep and shallow implant depth profiling of ions in Si measured with secondary ion mass spectroscopy (SIMS) and photoluminescence (PL) spectral measurements were carried out at room temperature via a Laser Raman Spectrometer with a He-Cd laser excitation frequency of 325 nm. The nature of various chemical bonds between silicon, phosphorous, oxygen, nitrogen, hydrogen atoms was studied using Fourier transform infrared (FTIR) spectroscopy (JASCO IRT-5000 Series) in the wavenumber range of 400–4000  $\text{cm}^{-1}$  in the attenuated total reflection (ATR) mode. The photoreflectance (PR) of the fabricated cells was measured using a UV-VIS-NIR spectrophotometer (MPC 3100, SHIMADZU). The quantum efficiency was measured using an IPCE System (QEX7) with a Xenon arc lamp that converts the incident photons to current. We studied the Ohmic contact of the solar cell, radiative recombination, and structural defects (cracks and line defect) due to implantation using electroluminescence (EL) images (McScience Inc., Model-K3300). Furthermore, we measured the minority carrier lifetimes (MCLT) using a  $\mu$ -PCD (SEMLAB WT2000) system with a 904 nm laser diode source and current-voltage (I-V) characteristics of the cells using a solar simulator (McScience Inc., K3000) under the standard testing condition.

## 3. Results and discussion

We utilized the SRIM-2013 simulation to determine the optimal implantation energy of oxygen ions. The implanted ions are responsible for structural modifications in the surface and bulk due to bond breakage and oxidation processes at a specific level of depth. Since the PECVD deposited  $\text{Si}_3\text{N}_4$  layer has a broad density range of 2.2–2.9  $\text{g}/\text{cm}^3$  [13], we simulated implantation energies of 10, 16, 26, 30, and 50 keV with the average density value of 2.6  $\text{g}/\text{cm}^3$  for the ARC thickness of 80 nm in the highly  $\text{H}_2$  diluted process as shown in Fig. 2(a–e), respectively. The expected ion trajectories versus target depth were simulated in XY

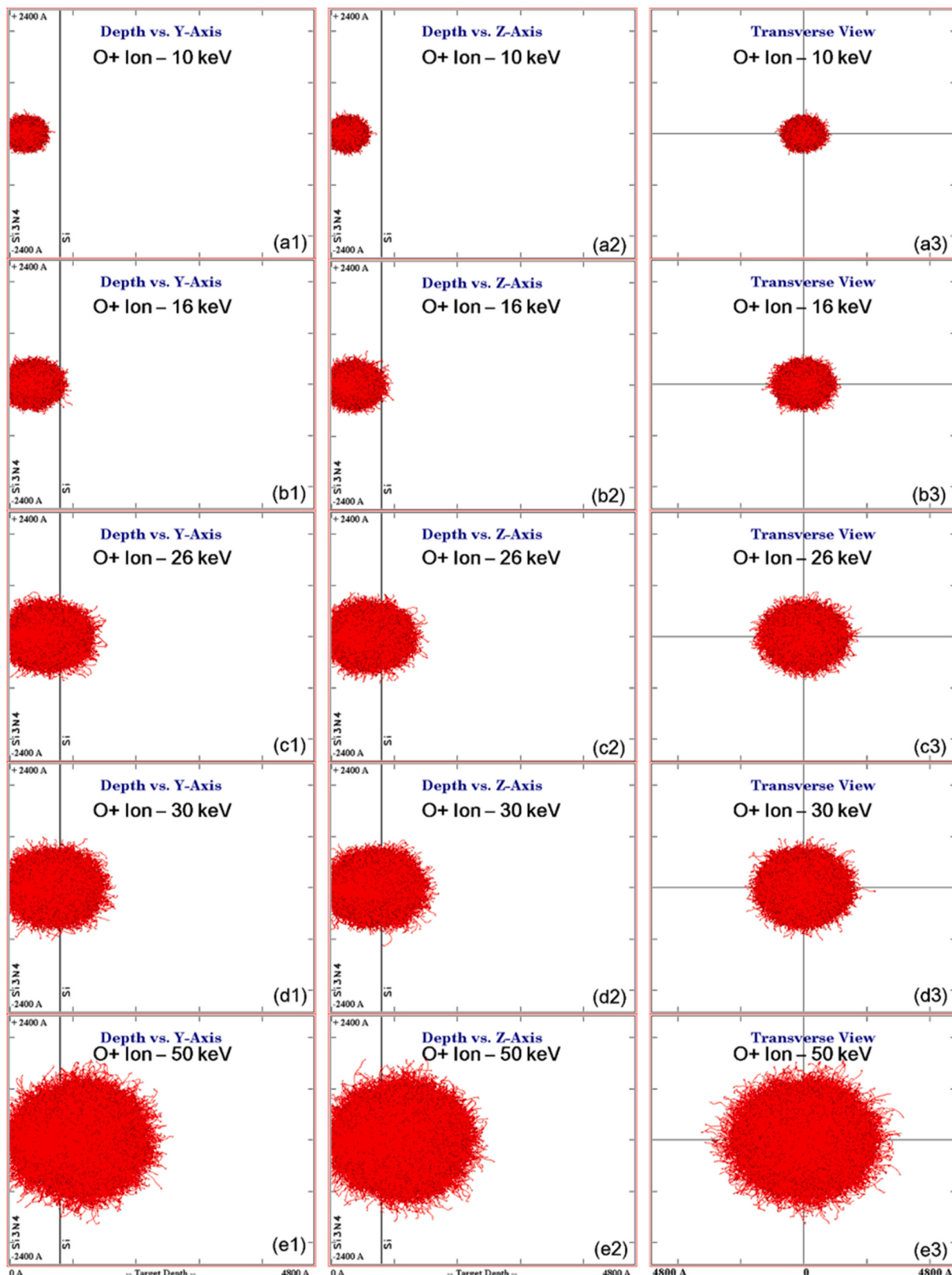


**Fig. 2.** Distribution of implanted oxygen ions projected at different planes with different implantation energies of 10, 16, 26, 30, and 50 keV.

longitudinal, YZ longitudinal, and XZ lateral distributions, as shown in Fig. 2 (a1-e1), (a2-e2), and (a3-e3), respectively. The X-axis is the depth axis, whereas the Y- and Z-axes are orthogonal to the X-axis. The mean projected range of all ions on the X-axis suggests that most ions are

located at the expected depth. The oxygen ions with 10 keV energy showed a penetration depth of 23.5 nm for the irradiated  $\text{Si}_3\text{N}_4$  layer. As energies increased with 16, 26, 30, and 50 keV, the penetration depths into the Si layer increased to 36.1, 57.3, 66.2 and 111.5 nm,

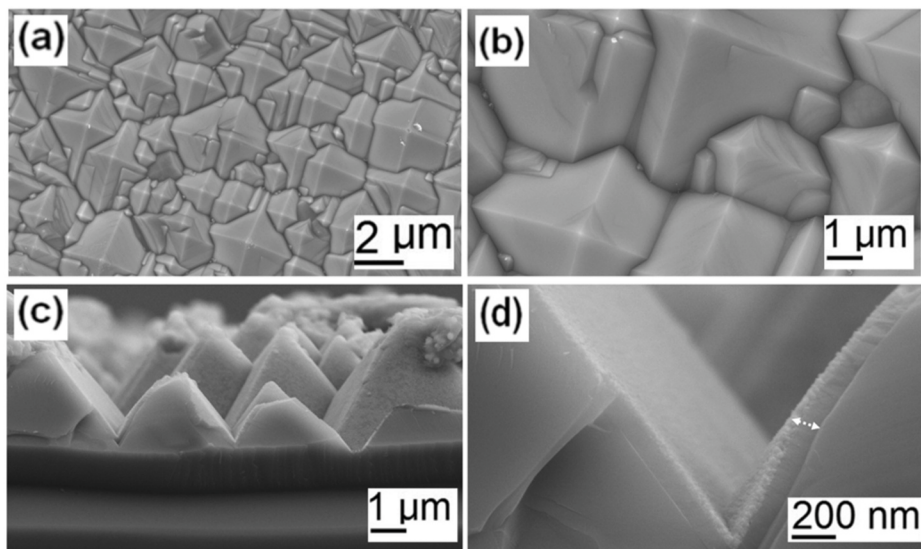


**Fig. 3.** FE-SEM images on (a, b) planar views and (c, d) cross-sectional views of the oxygen ion implanted sample with an energy of 16 keV at a dose of  $2 \times 10^{14}/\text{cm}^2$ . The  $\text{SiN}_x$  layer of micropyramidal surface was strongly damaged on the top region.

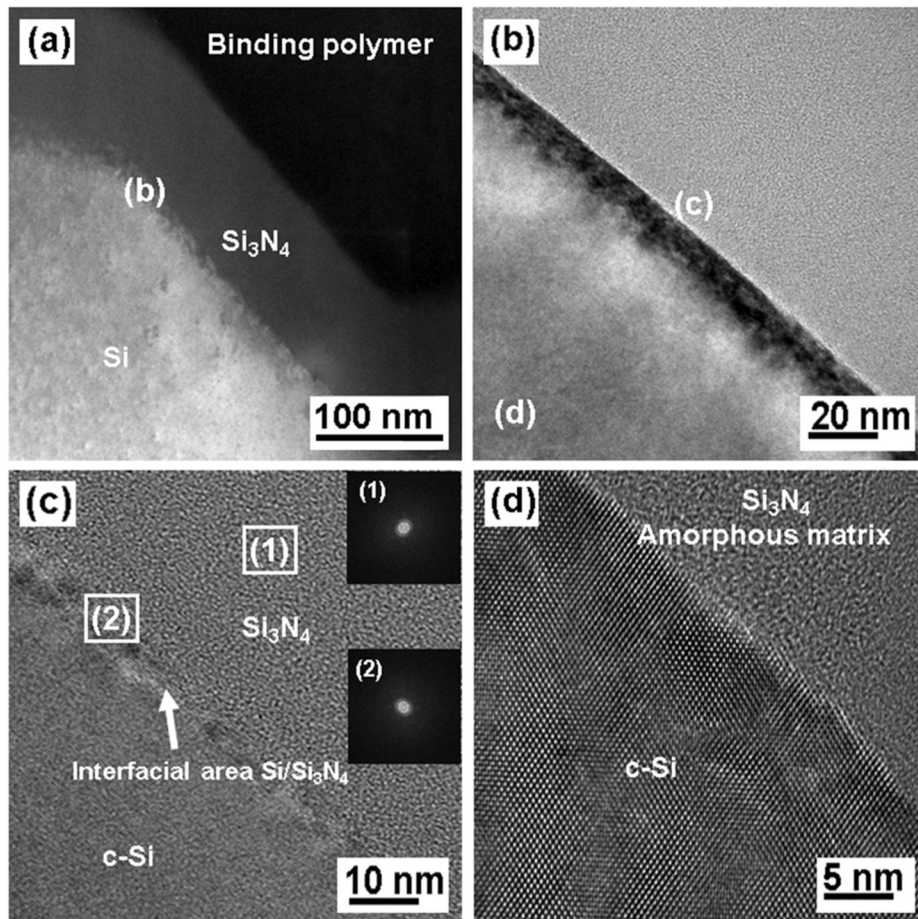


**Fig. 4.** Cs-corrected TEM images of reference cell on interfaces between  $\text{SiN}_x$  film and silicon substrate before ion implantation. The interface shows a dark contrast spot region with edge residual stress and the high-resolution image shows the clear interfacial change in morphology of the amorphous  $\text{SiN}_x$  layer and bulk c-Si.

respectively.

The ion irradiation parameters like stopping power, the average projected range, and ion straggling were simulated using the SRIM simulation code [14] for oxygen ion implantation on the  $\text{SiN}_x$  surface.

The profile depth distribution of ion implantation depends on the dose, energy, and type of ions, and the target material [15–17]. As is evident from SRIM calculations, a 16 keV energy is sufficient to reach the exact  $\text{SiN}_x/\text{Si}$  interface to form an insulation layer. At the same time, damage

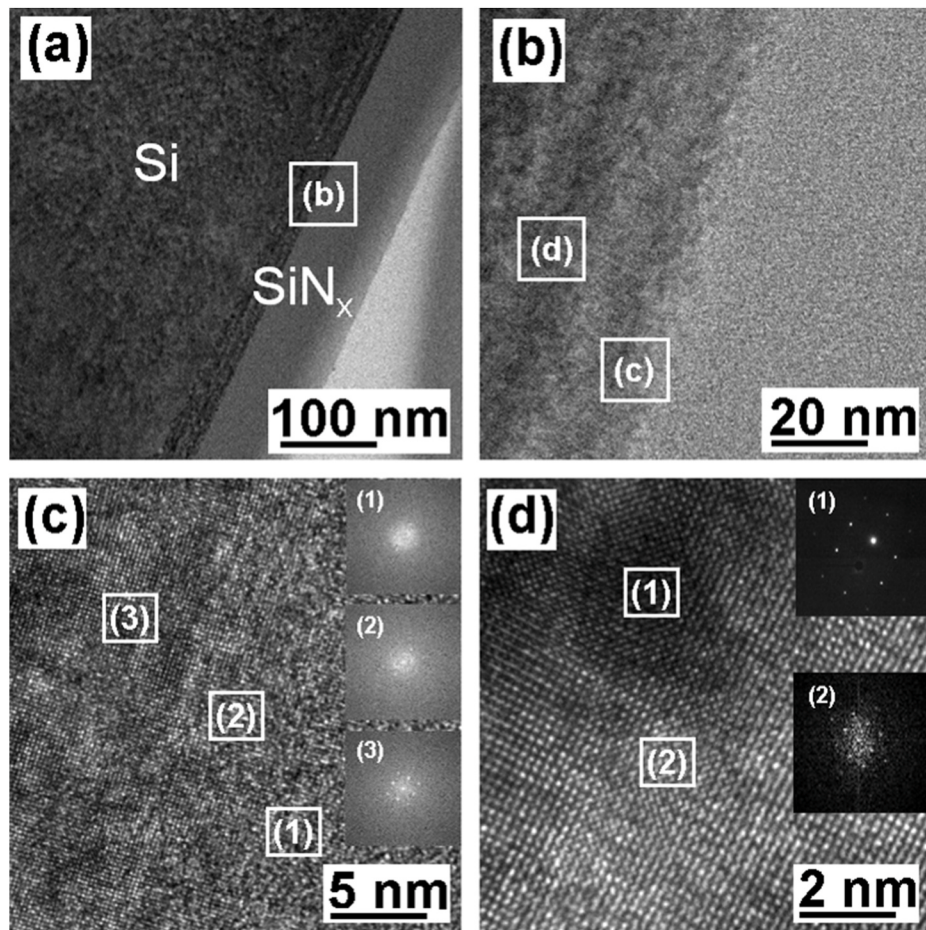


**Fig. 5.** Cs-corrected TEM image of the 16 keV oxygen ion implanted sample. The  $\text{SiN}_x/\text{Si}$  interface shows a contrast thin layer, where the oxygen ion implantation changes the structural morphology. The implantation results in Si surficial damage with stress contrast and the interfacial line is not clear.

and increased penetration depth in the  $\text{SiN}_x$  surface were found due to highly energetic oxygen ions. The cell implanted with energies of 30 and 50 keV ions damaged the surface compared to the 10 and 26 keV oxygen ions. According to SRIM-simulations, the cell implanted with oxygen ions with energies of 16 keV can just penetrate the  $\text{SiN}_x/\text{Si}$  interfacial layer.

FE-SEM was used to investigate the surface morphology of oxygen ion-implanted Si solar cells as shown in Fig. 3. The images in Fig. 3(a and b) show the morphology of oxygen ions on the top of the Si layer implanted with an oxygen ion energy of 16 keV and a dose of  $2 \times 10^{14}/\text{cm}^2$ . A thin layer can be seen in the center portions of the upper part of the pyramidal surface due to oxygen ion implantation as shown in Fig. 3(c). The post-ion-implanted thin films exhibited distinct grains on the Si surface. The ion-implanted thin film thickness was measured to be 48 nm by scanning the tilted sample cross-sectional view as shown in Fig. 3(d). However, the grain boundaries were not sharp, which can be attributed to the low order of the silicon oxide phase. On the other hand, the thin film implanted with an oxygen ion energy of 16 keV exhibited nanoparticles with well-defined grain boundaries. Further, the observation of well-defined grain boundaries is clarified by Cs-TEM measurement on Si nanoparticles of the silicon oxide phase, which is also consistent with the PL studies.

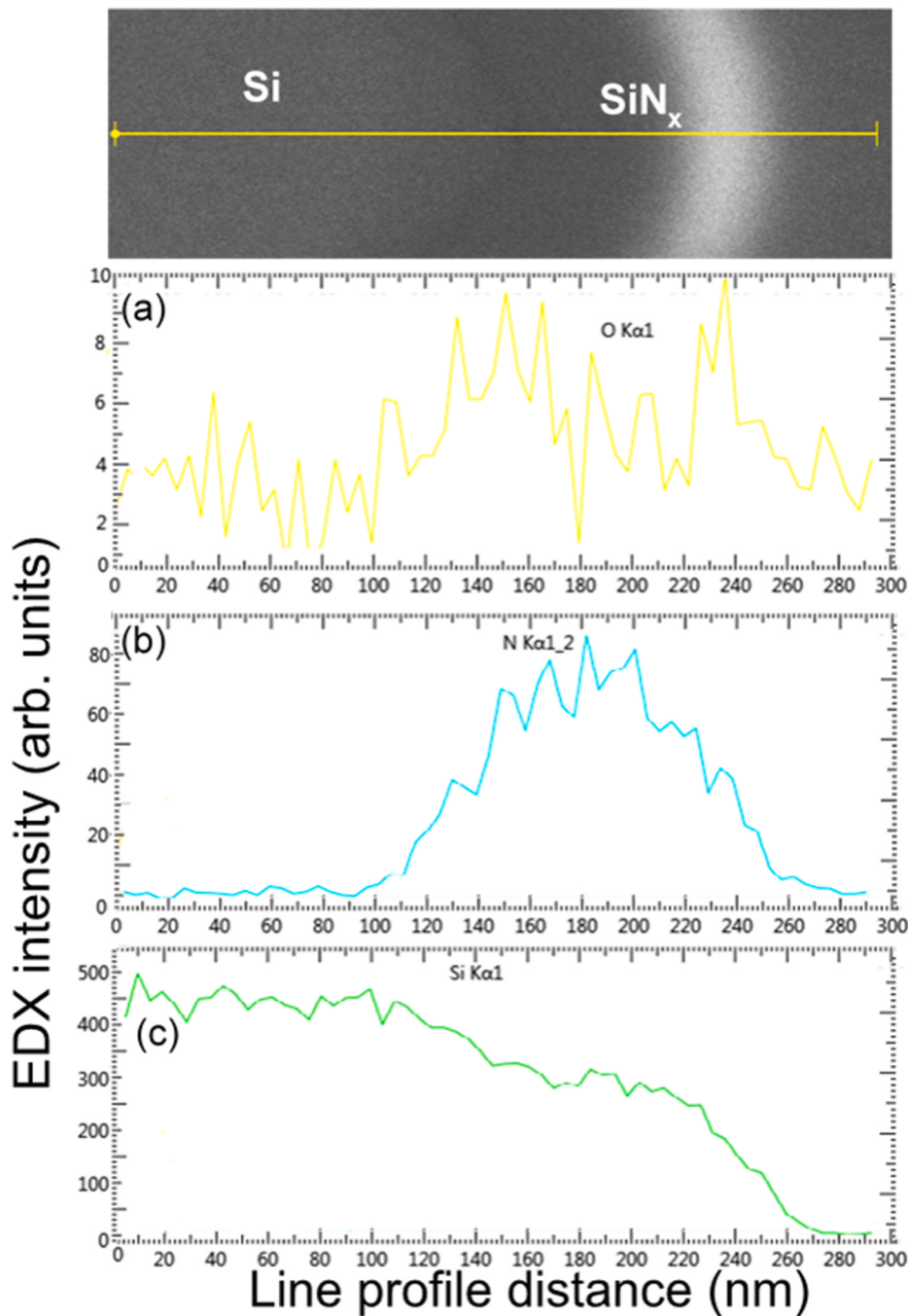
Fig. 4 shows the Cs-TEM images of the without implantation process sample (reference sample). From this sample, a  $\text{SiN}_x$  and  $\text{SiN}_x/\text{Si}$  interfacial layer is observed although the interface is also seen very clear. As depicted, the solar cell device was fabricated directly on a p-Si substrate, followed by 80 nm thick  $\text{Si}_3\text{N}_4$  dielectric layer as shown in Fig. 4 (a).

Fig. 4(b), (c), and (d) shows zoomed images into the interface region of

Si- $\text{SiN}_x$  layers. The Cs-TEM images verify that all the samples are in an amorphous phase  $\text{SiN}_x$  layers. Fig. 4(c) is a Cs-TEM image of the as-deposited sample that shows that the structure of the  $\text{SiN}_x$  film is clearly amorphous. The highly magnified image shows that the  $\text{Si}-\text{SiN}_x$  interfacial area remains unchanged, no nanocrystal formation and the Fourier transformed (FFT) pattern indicates its clearly amorphous region as shown in Fig. 4(d).

Fig. 5 shows the morphology of Cs-TEM images of the interface layer between the  $\text{SiN}_x/\text{Si}$  in p-Si solar cells when ion-implanted with oxygen ions at an energy of 16 keV. The protective ARC ( $\text{SiN}_x$ ) layer used during the TEM sample preparation is composed of amorphous phases. However, after oxygen ion implantation, an additional sublayer is seen at a depth of approximately 20–25 nm in Fig. 5 (a) beneath the  $\text{SiN}_x$  surface layer. Fig. 5 (b) shows a thin insulating wall observed in  $\langle 111 \rangle$  planes by oxygen ion implantation at the  $\text{SiN}_x/\text{Si}$  interface. The high magnification Cs-TEM image of the refined sublayer in Fig. 5 (c) reveals that the lattice fringes were slightly disordered, indicating crystal defects. Specifically, fewer diffraction rings and darker diffraction spots were observed closer to the amorphous sublayer. As a whole, the amorphous sublayer mainly consisted of a nanocrystalline and an amorphous phase, wherein the crystal planes were disordered, and the atom arrangement was low. The presence of a nanocrystalline structure or the amorphous phase is consistent with the broadened halo observed in the selected area electron diffraction pattern in Fig. 5 (d). Hence, the oxygen ion implantation produces a modification in the  $\text{SiN}_x/\text{Si}$  interface. The Cs-TEM analysis shows the nanocrystalline structure formed below the  $\text{SiN}_x$  layer.

Fig. 6 shows line mapping of  $\text{SiN}_x/\text{Si}$  interface layers in the oxygen



**Fig. 6.** EDX profiles of the 16 keV oxygen ion implanted sample along with the line-scale profile of oxygen, nitrogen, and silicon atoms. (For interpretation of the references to colour in this figure legend, the reader is referred to the Web version of this article.)

ion-implanted Si solar cells for 16 keV energy with a dose of  $2 \times 10^{14}/\text{cm}^2$  using energy-dispersive spectroscopic analysis. In the mapping, O, N, and Si atoms were found to be present with a very weak intensity of O atoms in Fig. 6(a) and large intensities of N atoms in Fig. 6(b) and Si atoms in Fig. 6(c). The strongly overlapped lines of N and Si atoms show the formation of the SiN<sub>x</sub> layer. The highly fluctuating curve of O atoms just after the implantation shows an unclear location and suggests that the formation of the silicon oxide layer is not clear. However, the fluctuating O atom distribution shows the implantation location at the SiN<sub>x</sub>/Si interfacial region.

The most significant result is that the oxygen ions swell the SiN<sub>x</sub> layer and form an insulation layer at the SiN<sub>x</sub>/Si interface, which is consistent with the SRIM simulation for the energy of 16 keV. Furthermore, the Cs-

TEM results showed a thin implanted layer near the interfacial region. To avoid the ion channeling effect, the oxygen ion implantation process was carried out at a tilt angle of 7° off the <100> direction. Thus, the oxygen ion beam passed through and stopped at the Si layer by breaking bonds on the whole traveled region. A mixed-phase of a-Si and damaged c-Si structures showed that the oxygen ion implantation formed a thin oxide layer [18,19]. The quantitative oxygen ion profile at the SiN<sub>x</sub>/Si interface can be further analyzed by investigation of SIMS measurements.

Fig. 7 shows the SIMS depth profiles of the reference sample of a Si solar cell and the cell sample with oxygen ion implantation at an energy of 16 keV. The reference sample before the implantation process in Fig. 7 (a) shows the SIMS depth profile of P, B, O, and N concentrations in the

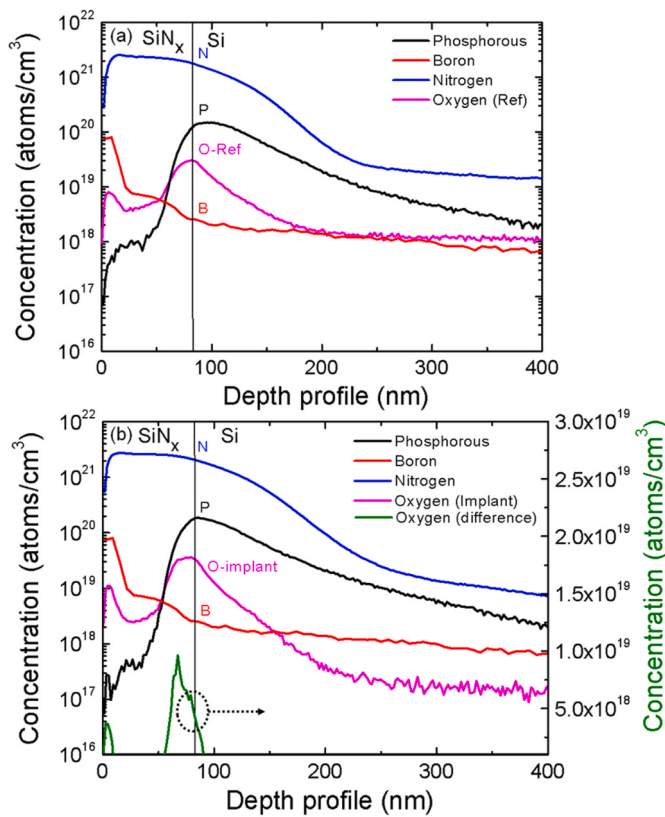


**Fig. 7.** SIMS depth profiles of phosphorus, boron, oxygen, and nitrogen concentration in the Si emitter region of the reference cell and implanted cell at an energy of 16 keV. The oxygen difference curve of implanted oxygen ions shows the oxygen distribution at the SiN<sub>x</sub> surface and SiN<sub>x</sub>/Si interface at the SiN<sub>x</sub> ARC depth of 80 nm.

emitter of Si solar cells. The N concentration due to SiN<sub>x</sub> ARC layer with a co-firing thermal process exponentially dropped at the interface, indicating the interfacial Si–N bonding character. The P concentration due to the POCl<sub>3</sub> diffusion process increased at the interface and exponentially dropped after forming the pn junction around a depth of 500 nm. The p-type Si wafer shows the B depth profile and shows the segregation at the SiN<sub>x</sub> surface due to the co-firing thermal process. The reference sample also shows an oxygen ion concentration of  $3.0 \times 10^{19}/\text{cm}^3$  at the Si surface, which may involve the POCl<sub>3</sub> diffusion process by forming the PSG layer. The Si sample implanted at an energy of 16 keV and an oxygen ion dose of  $2 \times 10^{14}/\text{cm}^2$  in Fig. 7 (b) shows similar ion profiles with increased oxygen concentration at the SiN<sub>x</sub>-side interface. The implanted samples of oxygen ion concentration show a little increase to  $3.8 \times 10^{19}/\text{cm}^3$  in Fig. 7 (b).

The increased O ion concentration is about 26.6%, which is marginal because the SIMS machine we used (CAMECA, 6F) has a 0.4–2.3% reproducibility error. This is not clear evidence of the oxygen species by implantation, but the trend is preferable. The subtracted oxygen content is the order of  $8.4 \times 10^{18}/\text{cm}^3$  at the interface. The increase in O ion concentration at the SiN<sub>x</sub>/Si interface due to the implantation is consistent with the SRIM simulation at an implantation energy of 16 keV. Furthermore, the Cs-TEM image in Fig. 5 indicates that the morphological change at the Si emitter-side interface is due to the O ion implantation. Therefore, the Si solar cells in the standard cell process have interfaces of emitter dead layers of P<sup>++</sup> doping with O and N concentrations caused by the POCl<sub>3</sub> diffusion process and thermal co-firing process of the SiN<sub>x</sub>/Si interfacial layer. The dead layer is important for Ag pastes to obtain good Ohmic contact with low series resistance. However, the dead layer also serves as a carrier recombination center and results in the reduction of the short circuit current. The

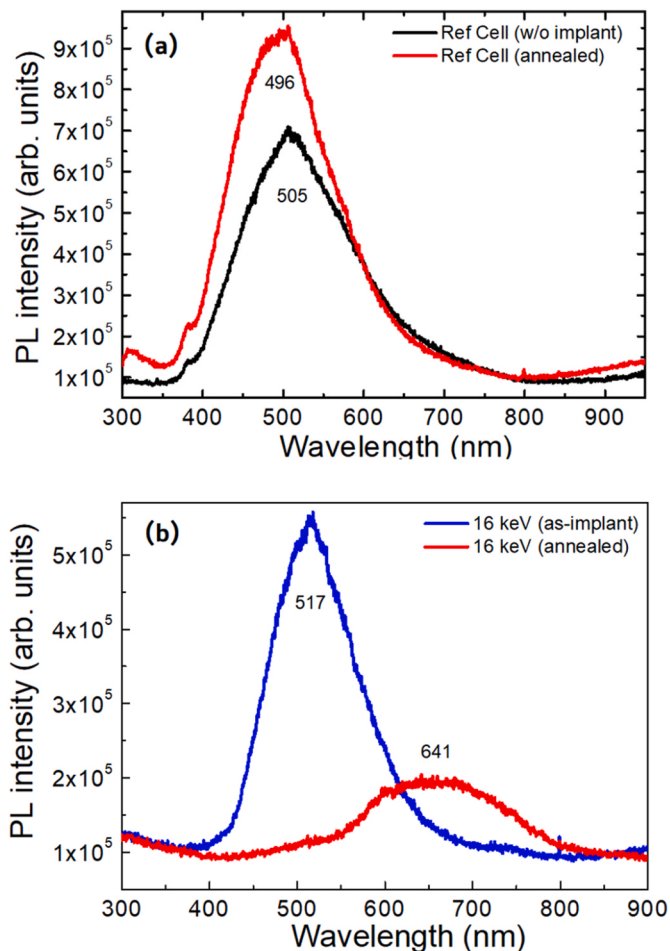


**Fig. 8.** Photoluminescence spectra of the Si solar cells for (a) the reference samples and (b) the samples of oxygen ion implantation with an energy of 16 keV. The subsequent annealing process was carried out for both samples at 850 °C in a N<sub>2</sub> ambient for 30 s.

implantation of the dead layer by O atoms breaks the Si lattice matrix and forms nanocrystallites [20]. A highly defective dead layer due to the implantation may contain a large concentration of oxygen atoms trapped on nanocrystallite defects. To clarify the oxygen species being introduced by implantation at the Si surface, it is valuable to measure the optical luminescence for the formation of nanocrystallites for the annealed sample.

Photoluminescence spectra for the reference cell and the samples implanted with oxygen ion at an energy of 16 keV with and without a post-implantation annealing process at 850 °C in N<sub>2</sub> ambient for 30 s as shown Fig. 8 (a) and (b), respectively. The reference cell with the SiN<sub>x</sub> layer showed PL spectra of visible broadband with the wavelength range of 400–650 nm. After the annealing process, the reference cell with a peak wavelength of 505 nm showed enhanced PL intensity with a tiny peak shift to a wavelength of 496 nm. The sample implanted at 16 keV also showed a similar PL peak at a wavelength of 517 nm. After the annealing process, however, the implanted cell showed a lowered peak with the spectral shift to the wavelength range of 550–800 nm. PL spectra of the oxygen ion implanted sample are sensitive to temperature. Therefore, the annealed sample of the oxygen ion-implanted cell had a different PL from the SiN<sub>x</sub> layer of the reference cell.

The SiN<sub>x</sub> layer in the reference cell provides nanostructured a-SiN<sub>x</sub> grains and Si nanocrystallite formation in the PECVD process and the subsequent annealing process [21,22]. The oxygen ion-implanted cell showed a PL peak at 517 nm corresponding to photon energies of 2.4 eV, which are similar to the reference cell. This implies that the SiN<sub>x</sub>-related

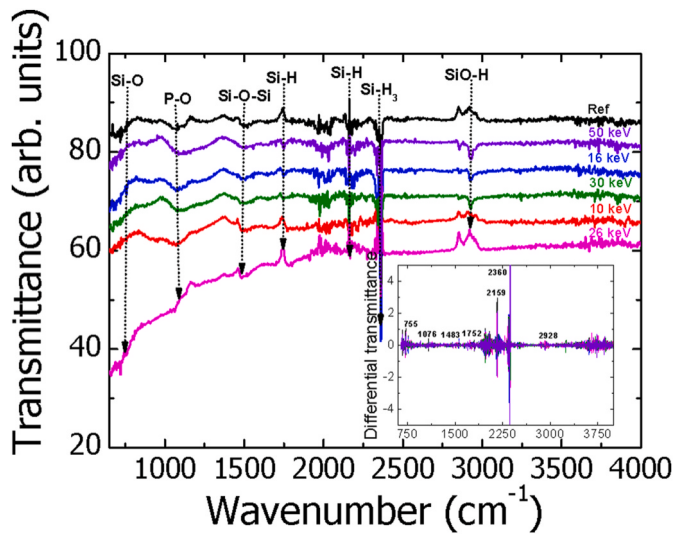


**Fig. 9.** Surface binding mechanism of oxygen ion implanted sample and reference cell. The sample was implanted with oxygen ions at various energies of 10, 16, 26, 30, and 50 keV. The inset shows the differential transmittance providing various peak positions. The surface attachment was probed using ATR-FTIR.

PL is dominant even in the oxygen ion-implanted cell. However, the annealed sample with the PL peak at 641 nm corresponding to photon energies of 1.93 eV showed a different luminescence from the annealed sample of a reference cell. This would be expected from quantum-confined Si nanoparticles due to the oxygen implanted Si region [23]. The PL of Si nanocrystallites for samples synthesized by Si implantation in a  $\text{SiO}_x$  matrix typically shows peaks at wavelengths around 650–880 nm (1.4–1.9 eV), depending on their size [24]. The implanted sample of Si nanoparticles embedded in the  $\text{SiO}_x$  matrix showed light absorption by Si nanoparticles and energy transfer into the oxide defect states. However, the annealed sample absorbs and emits light through Si nanoparticles [25]. These results indicate that the PL spectrum for the annealed oxygen ion Si samples is different from the reference cell and most likely originates from Si nanoparticles embedded in the  $\text{SiO}_x$  matrix.

The surface composition of the six different samples was characterized by ATR-FTIR transmittance analysis. The results are depicted in Fig. 9. The ATR-FTIR transmittance spectra of the virgin silicon and the oxygen ion-implanted samples were similar, showing a transmission peak at  $755\text{ cm}^{-1}$ , attributed to the Si–O stretching. The P–O stretches usually appearing at  $1000\text{--}1100\text{ cm}^{-1}$  were observed at  $1076\text{ cm}^{-1}$  as a broad transmittance peak due to phosphorus species. A large decrease of the P–O peaks phosphorous component indicates the presence of tridentate coordination, which is most favorable due to the resonance stabilization when all three O atoms bind to the P-silicon surface. ATR-FTIR analysis showed the binding of the tridentate configuration phosphine oxide to the surface through P–O bonds. Additionally, the cells show various absorption spectra of Si–O–Si, Si–H, Si–H<sub>3</sub>, and SiO–H bonds. The differential transmittance provides peaks at 1483, 1752, 2159, 2360, and  $2928\text{ cm}^{-1}$ , as shown in the inset. The oxygen ion-implanted cells with energies of 10, 16, 30, and 50 keV showed an increase in transmittance compared to the reference cell, but the cell implanted with an energy of 26 keV showed lower transmittance compared to the other implanted cells.

The transmission spectra showed a peak at  $755\text{ cm}^{-1}$  corresponding to the Si–O stretching frequency [26,27]. Since the absorption band of  $920\text{--}1088\text{ cm}^{-1}$  represents phosphate ester groups, the peaks at 975 and  $1070\text{ cm}^{-1}$  correspond to the P–O bonds [28], while those at 1752 and  $2159\text{ cm}^{-1}$  are assigned to the Si–H mode and  $2360\text{ cm}^{-1}$  associated with Si–H<sub>3</sub> bonds [27,29]. The transmission peak at  $2928\text{ cm}^{-1}$  was

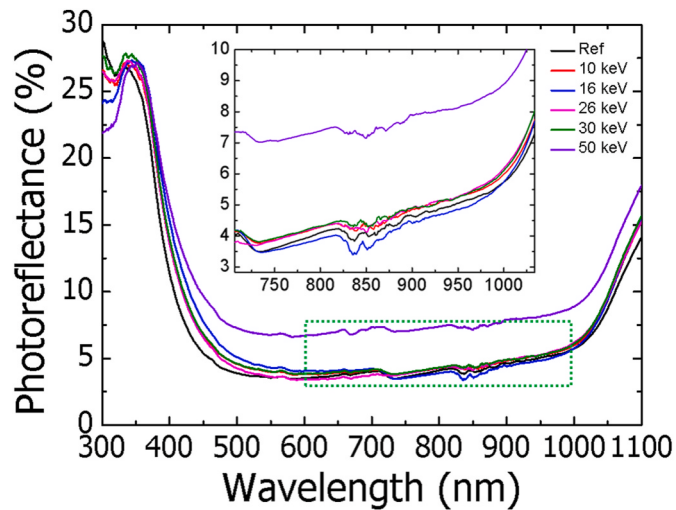


**Fig. 10.** Photoreflectance spectra of the reference cell and oxygen ion-implanted Si solar cells with energies of 10, 16, 26, 30, and 50 keV at a dose of  $2 \times 10^{14}/\text{cm}^2$ . The inset shows the magnified region in the wavelength range of 609–1016 nm.

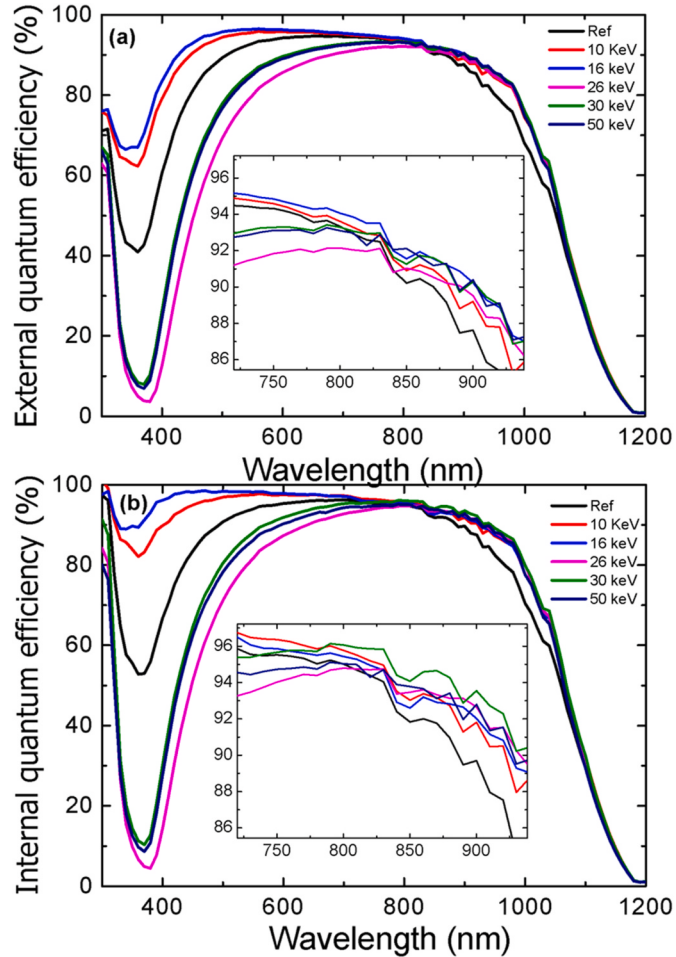


**Fig. 11.** The external and internal quantum efficiency of large area screen printed front junction n-type oxygen ion-implanted silicon solar cells with energies of 10, 16, 26, 30, and 50 keV and the reference cell. (For interpretation of the references to colour in this figure legend, the reader is referred to the Web version of this article.)

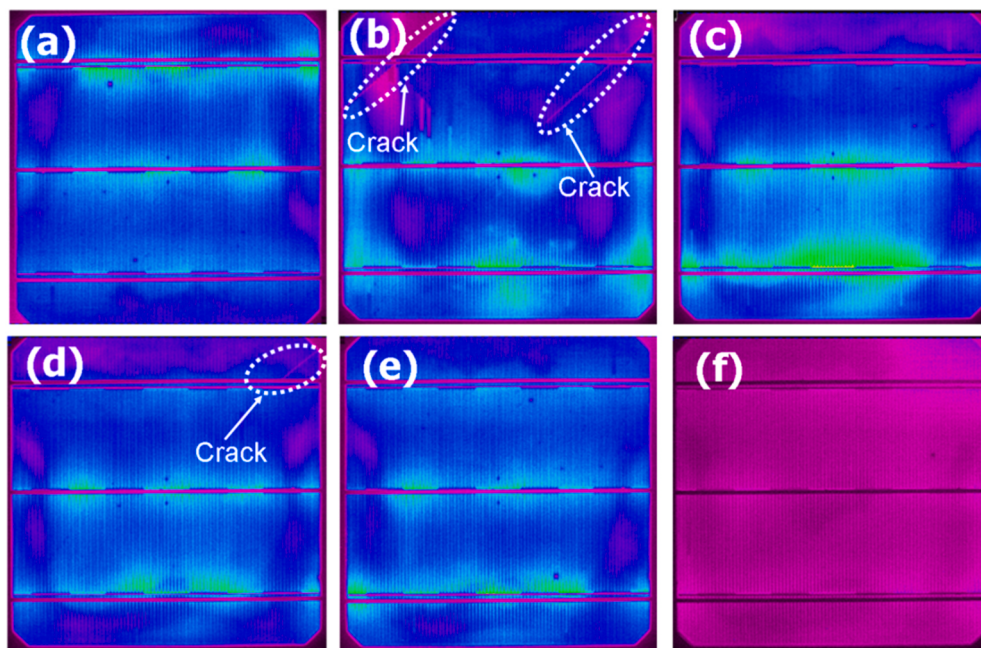


**Fig. 12.** Electroluminescence images of Si solar cells (a) reference, (b–f) the cell implanted with oxygen ions at 10, 16, 26, 30, and 50 keV at a dose of  $2 \times 10^{14}/\text{cm}^2$ , respectively.

assigned to the  $\text{SiO}-\text{H}$  bonds asymmetric bending vibration mode [27]. Typical FTIR spectra in the range  $650\text{--}4000\text{ cm}^{-1}$  of air and pure a- $\text{SiO}_x$  layer are shown, indicating that some vibrational modes of  $\text{Si}-\text{O}$  and oxygen incorporated molecules exist at the implanted surface. These results conclude that oxygen ions can change chemical bondings at Si surface rather than the formation of charged radicals. The effect of oxygen ion implantation on the PR per absorbed photon can be further confirmed by PR measurements.

Fig. 10 shows the PR of the oxygen ion implanted silicon solar cell measured over the wavelength range from 300 to 1200 nm after the cell fabrication process. The cells are implanted with oxygen ions at various energies of 10, 16, 26, 30, and 50 keV and a fixed dose of  $2 \times 10^{14}/\text{cm}^2$ . For the spectral range of 730–1005 nm, the implanted cell with 16 keV had a lower PR than other implanted cells and the reference cell. The reference cell had a lower PR than the other oxygen ion-implanted cells in the range of 346–522 nm, but the cell implanted with 26 keV had a lower PR in the range of 568–712 nm. The cell implanted with 10 and 30 keV energies showed a reduced PR compared to the high implantation energy of 50 keV. Furthermore, the reference cell has lower PR than the cell implanted with oxygen ions in the range of 1040–1100 nm.

The PR in the visible spectrum is not sensitive to the implantation of oxygen ions. However, the PR in the sub-bandgap region decreases with an increase in the oxygen ion implantation energy. There is reduced PR in the near-infrared region (NIR). The presence of defect layers is the cause for the decrease in the PR [30]. However, the reduced PR of the cell implanted with low energy 16 keV in the NIR shows that effective surface treatment is achieved by minimizing the carrier reduction at the surface of c-Si [31,32]. The effect of oxygen ion implantation on the photocurrent generation per absorbed photon can be confirmed by the external and internal quantum efficiency (EQE and IQE) measurements.

Fig. 11 (a) shows the EQEs of the reference and oxygen ion-implanted cells measured under a Xenon arc lamp. At the visible wavelength of 560 nm, the cell implanted with 16 keV has a maximum EQE of 96.52%, whereas, at the same wavelength, the cells implanted with energies of 10 keV, 26 keV, 30 keV, 50 keV, and reference cell showed EQEs of 95.86%, 80.38%, 87.03%, 86.36%, and 93.44%, respectively. However, for the NIR region of 790 nm, the reference cell has an EQE of 93.66%, and the cells implanted with energies of 10, 16, 26, 30, 50 keV showed differences with EQE values of 93.93%, 94.34%,

92.13%, 93.44%, and 93.26%, respectively. In the UV region, the EQE showed enhancement in samples with implantation energies of 10 and 16 keV, but a decrease in the samples with 26, 30, and 50 keV compared to the reference sample. This indicates that the samples with 26, 30, and 50 keV are sensitive to the photo-response in the short-wavelength visible region.

The IQE was analyzed from the EQE and PR data for the reference and oxygen ion-implanted samples for various energies, as shown in Fig. 11 (b). IQE is defined as the carrier collection by the absorbed light. Since the photo-absorption coefficient ( $A$ ) is the subtraction of reflectance ( $R$ ) and transmittance ( $T$ ) from incident intensity coefficient ( $I = 1$ ), the following relationship holds:  $\text{IQE} = \text{EQE}/(1-R-T)$ . For the whole implanted cell, the IQE is enhanced in the whole spectral region compared to the EQE. At the visible wavelength of 471 nm, the cell implanted with 16 keV has a maximum IQE of 98.86%, whereas, at the same wavelength, the cells implanted with energies of 10, 26, 30, and 50 keV showed IQEs of 95.90%, 61.57%, 73.36%, and 70.74%, respectively. Compared to the reference cell, the samples implanted with energies of 10 and 16 keV showed IQE enhancement over the whole spectrum, but the reduced IQE in the samples implanted with 26, 30 and 50 keV in the UV-VIS wavelength region (300–733 nm) increased up to the NIR region.

The increased EQE of the cells implanted with energies of 10 and 16 keV with a dose of  $2 \times 10^{14}/\text{cm}^2$  indicates the passivation preventing the carrier recombination at the interfacial layer and an increase in the minority carrier diffusion length due to the reduced emitter layer by the oxygen ion implantation [33]. This indicates that the carrier recombination is reduced in the dead layer. However, the cells implanted with oxygen ion energies of 26, 30, and 50 keV showed a lower EQE than the reference cell. This phenomenon is strange and may cause a decrease in photocurrent by damaging the emitter layer [34,35]. We further analyze the cells for EL measurement to confirm the behavior of carrier generation due to the oxygen ion implantation.

Fig. 12 shows the EL images of the reference and various energies of the oxygen ion-implanted Si solar cells. The reference cell shows a bright EL image with dark lines under many finger lines in the surface and edge area as shown in Fig. 12 (a). Fig. 12(b–f) shows that with increasing implantation energy, the EL image brightness decreases continuously for the energies of 10, 16, 26, 30, and 50 keV oxygen ion-implanted cells.

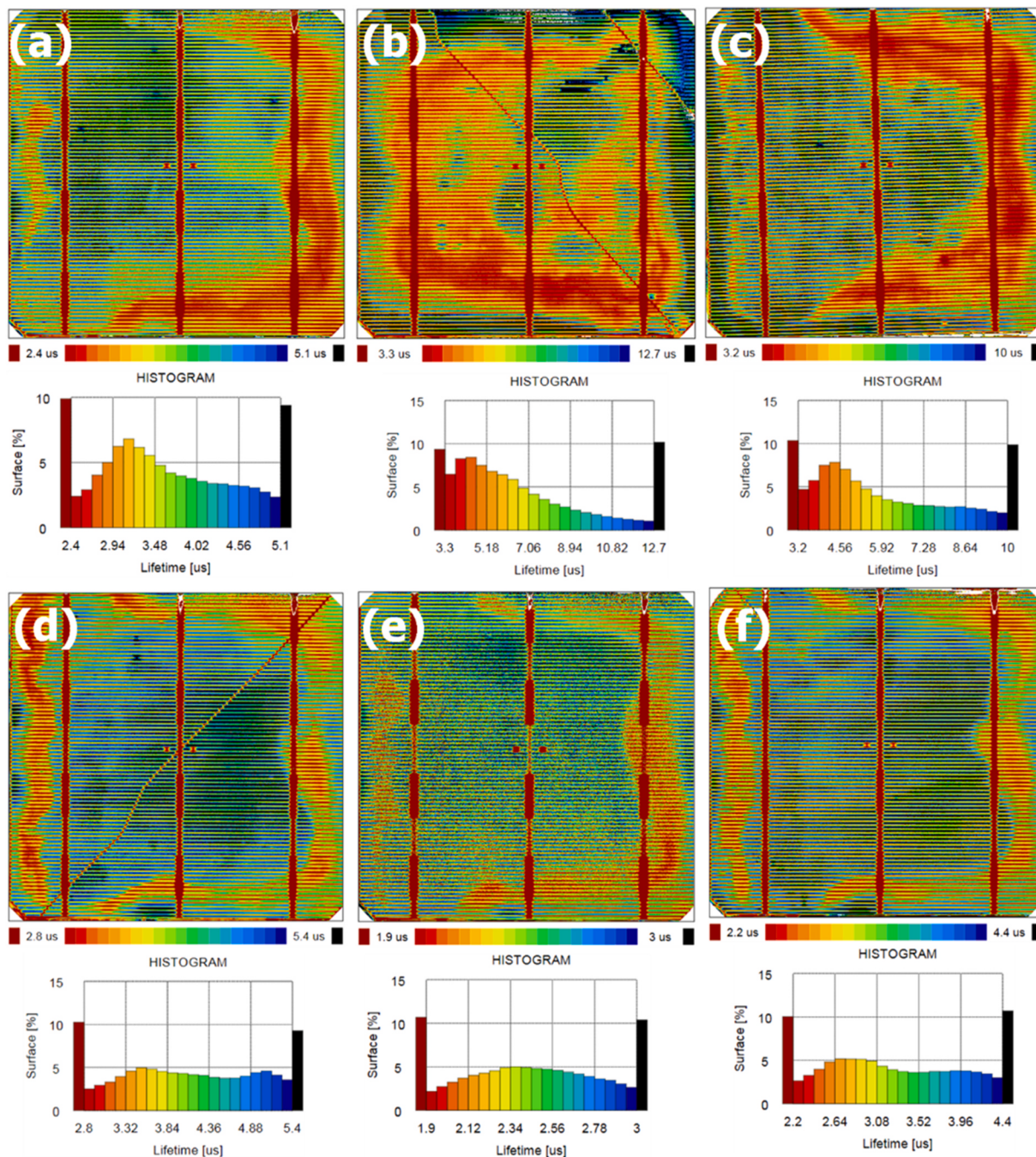


**Fig. 13.** Distribution of minority carrier lifetime for (a) reference cell and the cells implanted with oxygen ions at various energies, (b–f) 10, 16, 26, 30, and 50 keV at a dose of  $2 \times 10^{14}/\text{cm}^2$ , respectively.

The cell implanted with low energy of 16 keV has a brighter EL image than the cells implanted with 26–50 keV energies. The cells implanted with 10 and 26 keV show crack and broken finger lines in Fig. 12(b–d). The number of dark spots increased with increasing oxygen ion implantation energy, revealing that the cells treated with high energy will show surface damage and degrade cell performance. Therefore, we conclude that the increased oxygen ion implantation energies of 30 and 50 keV provide a darker EL image with more significant surface damage as shown in Fig. 12(e and f).

Normally, the EL image is related to the p-n junction as characterized by the shunt resistance ( $R_{sh}$ ) and the metal-semiconductor interface Ohmic contact, characterized by series resistance ( $R_s$ ) [36,37]. The ion implantation induced surface damage and reduced the EL image

brightness. The darkness of EL images indicates the formation of defects in the solar cells via the excess energy of oxygen ion implantation that degrades the cell performance with a lowered short circuit current density due to current leakage across the pn junction [38,39]. The EL images of the cell implanted with an energy of 16 keV is superior to the other oxygen ion-implanted cells as well as the reference cell, which indicate that low energy oxygen ion implantation is required to prevent carrier reduction from the surface after the formation of an insulation layer to enhance the cell efficiency.

Fig. 13 shows the minority carrier lifetime of the oxygen ion-implanted Si solar cells. Fig. 13(a) shows the distribution percentage of minority carrier lifetimes for the reference cell and the cells implanted with energies of 10–50 keV at a dose of  $2 \times 10^{14}/\text{cm}^2$ , respectively, as

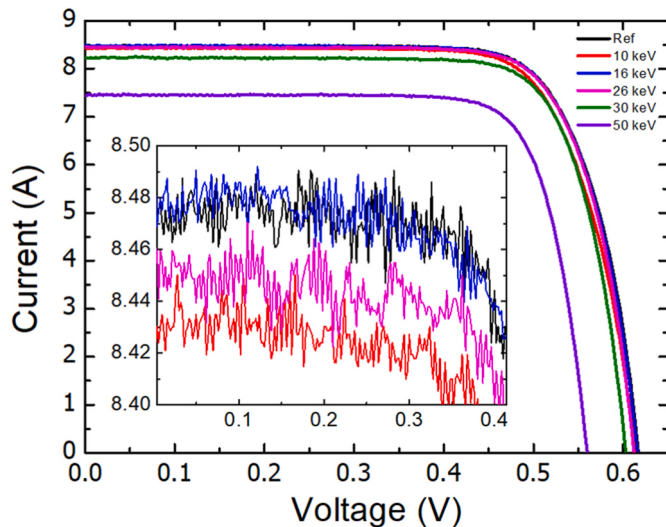


**Fig. 14.** Current-Voltage (I-V) curves of 17.14% efficient screen-printed cell featuring oxygen ion-implantation at energies of 10, 16, 26, 30, and 50 keV and the reference cell measured using a solar simulator at 1-Sun under AM 1.5 G spectrum with an irradiance of  $1000 \text{ W/m}^2$  at room temperature. The inset shows the magnified region in the voltage range of 0.03–0.42 V.

shown in Fig. 13 (b)–(f). The average value of the effective minority carrier lifetime of the reference cell is  $3.65 \mu\text{s}$  in the range of  $2.4\text{--}5.1 \mu\text{s}$ . The cell implanted with an energy of 16 keV at a dose of  $2 \times 10^{14}/\text{cm}^2$  has an average value of effective minority carrier lifetime of  $6.1 \mu\text{s}$  in the range of  $3.2\text{--}10 \mu\text{s}$ . The cells implanted with energies of 10, 26, 30, and 50 keV have average values of  $7.2 \mu\text{s}$  with a range of  $3.3\text{--}12.7 \mu\text{s}$ ,  $2.44 \mu\text{s}$  with  $1.9\text{--}3 \mu\text{s}$ ,  $4.07 \mu\text{s}$  with  $2.8\text{--}5.4 \mu\text{s}$ , and  $3.27 \mu\text{s}$  with  $2.2\text{--}4.4 \mu\text{s}$ , respectively. From the above results, we can see that the cell implanted with an energy of 10 keV has the highest minority carrier lifetime, which indicates a low concentration of oxygen ions within  $\text{SiN}_x$ , making it very effective for surface passivation.

However, when the implantation energy increased, the effective minority carrier lifetime decreased, which indicates that implanted oxygen ions induced surface defects and interfacial defects that act as recombination centers. These defects deactivate the dopant, leading to a change in the resistivity of the solar cell and act as carrier trapping centers [40]. Therefore, oxygen ions implanted with low energy in the  $\text{SiN}_x$  layer passivate the defects and reduce the defect-assisted recombination centers. In other words, it increases the minority carrier lifetime, thereby enhancing solar cell performance.

Fig. 14 shows the I-V curve for the reference and oxygen ion-implanted cells measured using a solar simulator at 1 Sun under AM1.5 G Sun spectrum and irradiation of  $1000 \text{ W/m}^2$ . The effective areas of these cells were the same at 6 inches. The electrical performance data of the reference cell and implanted cells are listed in Table 1. The solar cell parameters of the reference cell had a conversion efficiency ( $\eta$ ) of 16.89% with an open-circuit voltage ( $V_{oc}$ ) of 0.618 V, a short circuit current ( $I_{sc}$ ) of  $8.474 \text{ A}$ , and a fill factor (FF) of 75.97%. As seen in Fig. 14, the results reveal that  $I_{sc}$ , FF, and conversion efficiency are very

sensitive to the oxygen ion implantation, except for the cell implanted with a low energy of 16 keV and a dose of  $2 \times 10^{14}/\text{cm}^2$  that showed the highest cell efficiency of 17.14% with an  $I_{sc}$  of  $8.485 \text{ A}$ , a  $V_{oc}$  of  $0.616 \text{ V}$  and an FF of 77.39%.

Fig. 15 (a) shows the semi-logarithmic I-V plot of photocurrent subtraction from the short circuit current ( $I_{sh}-I_{ph}$ ) for a Si solar cell implanted with oxygen ion with various energies of 10, 16, 26, 30, and 50 keV and the reference cell. From the dark carrier transport analysis of  $I=I_0 \exp(qV/nkT)$  with increasing forward bias, the recombination current limitation changed to the minority carrier diffusion limitation at  $0.435 \text{ V}$ . At an open circuit voltage around  $0.6 \text{ V}$ , the series resistance at the neutral bulk n and p-type regions limits the current. The sample implanted at an energy of 10 keV shows the limitation of minority carrier diffusion compared to the reference cell, as shown in Fig. 15(b), indicating the decrease in cell efficiency. As shown in Fig. 15(c), the implanted sample at an energy of 16 keV showed improved recombination character by decreased current as compared to the reference sample, indicating improved cell efficiency. The implanted sample at an energy of 26 keV showed a change in the series resistance limitation compared to the reference sample, as shown in Fig. 15 (d), and showed decreased cell efficiency.

The oxygen ion implantation has a significant effect on the photovoltaic cell performance. As the ion implantation energies increased, the efficiency and open-circuit voltage decreased. For the lower implantation energy of 16 keV, the short circuit current, FF, and the minority carrier lifetimes increased. As the implantation energies increased, the defect densities on the emitter layer increased and acted as recombination centers for the majority charge carriers, enhancing the dark forward current and decreasing  $V_{oc}$  of the cells [41]. Furthermore, the  $I_{sc}$  and  $V_{oc}$  of the implanted cells decreased when the ion implantation energy increased, which indicates the existence of defect levels in the emitter region. The FF is related to both series and parallel resistances in equivalent circuit simulation [42,43]. For cells with a similar series resistance, the shunt resistance is the dominant factor and vice versa. Furthermore, the  $I_{sc}$  of the implanted cells decreases with an increase in the implantation energy, which shows the loss of the photo-generated charge carriers. Hence, the overall cell efficiency is reduced. Therefore, oxygen ion implantation at low energy of 16 keV is a suitable candidate to prevent carrier reduction from the surface trapping.

#### 4. Conclusions

In summary, we investigated oxygen ion implantation into Si solar cells. The implanted Si thin film shows the matrix fragmentation and the photoluminescence spectra. The morphological change showed an irregular pattern of diffraction intensity due to the formation of nanocrystallites. Among the samples with various implantation energies, the Si solar cell with an energy of 16 keV showed enhanced cell performance. This was achieved due to the inclusion of an oxygen ion on the Si solar cells interfacial region by oxygen ion implantation. The interfacial breakage of the optical window between fingerlines removed the high phosphorus content doped dead layer of the Si emitter. Silicon solar cells treated with oxygen ion implantation at an energy of 16 keV with a dose of  $2 \times 10^{14}/\text{cm}^2$  can block the carriers from surface trapping and minimize carrier reduction and improve the conversion efficiency. The

**Table 1**

Photovoltaic cell parameters of the oxygen ion-implanted Si solar cells with various energies and a dose of  $2 \times 10^{14}/\text{cm}^2$ . The represented values show the median values for conversion efficiency, and dispersion values come from the maximum and minimum values of three fabricated 6-inch Si solar cells.

Cell	$\eta$ [%]	FF [%]	$I_{sc}$ [A]	$V_{oc}$ [V]	$R_s$ [ $\Omega$ ]	$R_{sh}$ [ $\Omega$ ]
Ref.	16.89 (0/-0.2)	75.97 (0/-0.3)	8.474 (+0.051/0)	0.618 (0/-0.01)	0.0010 (+0.0006/0)	3.41 (+1.3/-0.81)
10 keV	16.64 (0/-0.45)	75.28 (+0.81/0)	8.448 (+0.012/-0.01)	0.613 (+0.001/-0.01)	0.0016 (+0.0004/0)	1.31 (+4.34/-0.25)
16 keV	17.14 (+0.32/-0.33)	77.39 (+0.19/-0.56)	8.485 (+0.008/-0.002)	0.616 (+0.001/0)	0.0014 (0/-0.0002)	2.69 (+3.21/-1.43)
26 keV	16.87 (0/-0.09)	76.93 (+0.13/-0.55)	8.458 (+0.001/-0.004)	0.612 (0/-0.002)	0.0009 (+0.004/0)	1.01 (+8.27/0)
30 keV	16.08 (0/-0.02)	76.41 (+0.84/-0.17)	8.224 (+0.012/0)	0.603 (0/-0.001)	0.0010 (0/+0.0001)	8.44 (+0.73/-7.42)
50 keV	13.68 (+0.06/-0.03)	75.44 (+0.12/-0.3)	7.443 (+0.02/-0.022)	0.559 (+0.001/-0.001)	0.0009 (+0.0001/0)	3.08 (+1.96/-1.91)

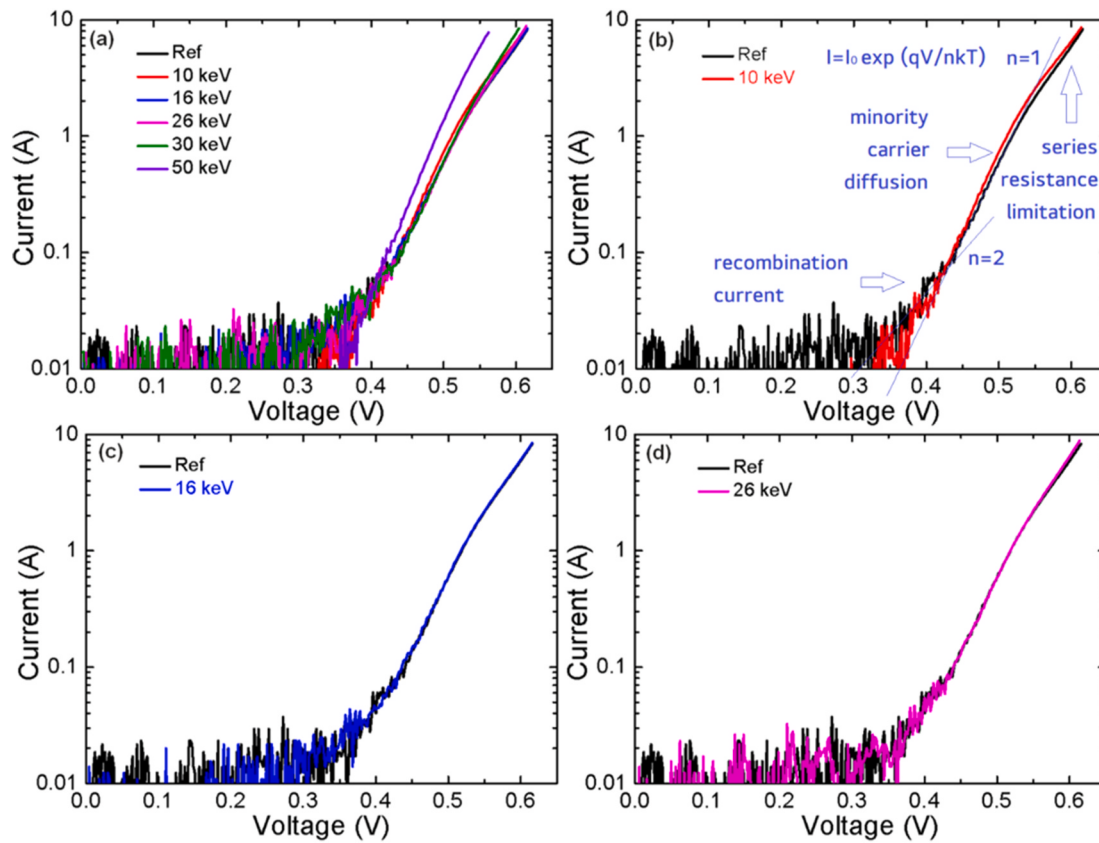


**Fig. 15.** Semi-logarithmic current-voltage (I-V) plot of photocurrent subtraction from the short circuit current ( $I_{sh} - I_{ph}$ ) for a Si solar cell implanted with oxygen ions with various energies of 10, 16, 26, 30, and 50 keV and the reference cell.

quantum efficiency in the cells at low energies 10 and 16 keV of oxygen ion implantation increased due to the broad range light absorption of the cell, indicating good surface passivation, showing increased efficiency and  $I_{sc}$ . However, the cells implanted with 26, 30, and 50 keV showed a reduction in quantum efficiency overall spectral regions due to the formation of surface recombination via defect levels when compared to the reference cell. Furthermore, the same set of cells implanted with 26, 30, and 50 keV showed an enhancement of photoreflectance throughout the NIR region, which led to a reduction in quantum efficiency. The conversion efficiency and the electrical parameters of the ion-implanted silicon solar cells degraded by increasing oxygen ion implantation above the energy level of 26 keV and more at the fluence of  $2 \times 10^{14} \text{ cm}^{-2}$ . Cell performance decreased as ion implantation energy increased, indicating the formation of defect-assisted surface recombination due to a decrease in the short circuit current and minority carriers. In conclusion, the cell implanted with low energy in the emitter layer of the solar cell provides an insulation layer for carrier passivation, enhancing the cell performance for better carrier management in the dead layer region.

#### CRediT authorship contribution statement

**Rajkumar Sahu:** Conception and design of study, Methodology and simulation, Acquisition of data and analysis, Writing – original draft. **Srikanta Palei:** Conceptualization and validation, Visualization and data curation, Writing – review & editing. **Keunjoo Kim:** Supervision, Resources, Funding acquisition, Writing – review & editing.

#### Declaration of competing interest

The authors declare that they have no known competing financial interests or personal relationships that could have appeared to influence the work reported in this paper.

#### Acknowledgments

The Basic Science Research Program supported this research through the National Research Foundation (NRF) of the Republic of Korea, funded by a grant from the Ministry of Education under (NRF-2016R1D1A1B03934923). The oxygen ion beam implantation was carried out at KAERI-KOMAC in Gyeongju, Republic of Korea.

#### References

- [1] J.Y. Lee, S.W. Glunz, Investigation of various surface passivation schemes for silicon solar cells, *Sol. Energy Mater. Sol. Cells* 90 (2006) 82–92.
- [2] B. Min, H. Wagner, A.D. Shirazi, A. Kammerle, H. Kurz, P.P. Altermatt, Heavily doped Si:P emitters of crystalline Si solar cells: recombination due to phosphorus precipitation, *Phys. Status Solidi RRL* 8 (2014) 680–684.
- [3] P. Ostoja, S. Guerri, P. Negrini, S. Solmi, The effects of phosphorus precipitation on the open-circuit voltage in  $N^+$ /P silicon solar cells, *Sol. Cell.* 11 (1984) 1–12.
- [4] J.F. Lelievre, E. Fourmond, A. Kaminski, O. Palais, D. Ballutaud, M. Lemiti, Study of the composition of hydrogenated silicon nitride  $\text{SiN}_x:\text{H}$  for efficient surface and bulk passivation of silicon, *Sol. Energy Mater. Sol. Cells* 93 (2009) 1281–1289.
- [5] S.W. Glunz, F. Feldmann,  $\text{SiO}_2$  surface passivation layers - a key technology for silicon solar cells, *Sol. Energy Mater. Sol. Cells* 185 (2018) 260–269.
- [6] G. Dingemans, M.M. Mandoc, S. Bordihn, M.C.M. van de Sanden, W.M.M. Kessels, Effective passivation of Si surfaces by plasma deposited  $\text{SiO}_x/\text{a-SiN}_x:\text{H}$  stacks, *Appl. Phys. Lett.* 98 (2011) 222102–222103.
- [7] J. Dupuis, E. Fourmond, J.F. Lelievre, D. Ballutaud, M. Lemiti, Impact of PECVD  $\text{SiON}$  stoichiometry and post-annealing on the silicon surface passivation, *Thin Solid Films* 516 (2008) 6954–6958.
- [8] J. Schmidt, A. Merkle, R. Brendel, B. Hoex, M.C.M. van de Sanden, W.M.M. Kessels, Surface passivation of high-efficiency silicon solar cells by atomic-layer-deposited  $\text{Al}_2\text{O}_3$ , *Prog. Photovoltaics Res. Appl.* 16 (2008) 461–466.
- [9] J. Cui, Y. Wan, Y. Cui, Y. Chen, P. Verlinden, A. Cuevas, Highly effective electronic passivation of silicon surfaces by atomic layer deposited hafnium oxide, *Appl. Phys. Lett.* 110 (2017) 21602–21605.
- [10] T.G. Allen, A. Cuevas, Electronic passivation of silicon surfaces by thin films of atomic layer deposited gallium oxide, *Appl. Phys. Lett.* 105 (2014) 31601–31604.
- [11] Z. Ling, J. He, X. He, M. Liao, P. Liu, Z. Yang, J. Ye, P. Gao, Excellent passivation of silicon surfaces by thin films of electron-beam-processed titanium dioxide, *IEEE J. Photo* 7 (2017) 1551–1555.

- [12] R.S. Bonilla, B. Hoex, P. Hamer, P.R. Wilshaw, Dielectric surface passivation for silicon solar cells: a review, *Phys. Status Solidi* 214 (7) (2017) 1700293.
- [13] A.E. Kaloyerous, Y. Pan, J. Goff, B. Arkles, Review-silicon nitride and silicon nitride-rich thin film technologies: state-of-the-art processing technologies, properties, and applications, *ECS J. Solid State Sci. Technol.* 9 (2020), 063006.
- [14] J.F. Ziegler, J.P. Biersack, M.D. Ziegler, The Stopping and Range of Ions in Solids, SRIM Software, 2008.
- [15] S.M. Malik, D.E. Muller, K. Sridharan, R.P. Fetherston, N. Tran, J.R. Conrad, Distribution of incident ions and retained dose analysis for a wedge-shaped target in plasma source ion implantation, *J. Appl. Phys.* 77 (1995) 1015–1019.
- [16] Y. Zhang, I.T. Bae, K. Sun, C. Wang, M. Ishimaru, Z. Zhu, W. Jiang, W.J. Weber, Damage profile and ion distribution of slow heavy ions in compounds, *J. Appl. Phys.* 105 (2009) 104901–104912.
- [17] R.E. Stoller, M.B. Toloczkko, G.S. Was, A.G. Certain, S. Dwaraknath, F.A. Garner, On the use of SRIM for computing radiation damage exposure, *Nucl. Instrum. Methods Phys. Res. B* 310 (2013) 75–80.
- [18] J.P. de Souza, C.A. Cima, P.F.P. Fichtner, H. Boudinov, Amorphization/recrystallization of buried amorphous silicon layer induced by oxygen ion implantation, *J. Appl. Phys.* 95 (2004) 877–880.
- [19] A. De Veirman, K. Yallup, J.V. Landuyt, H.E. Maes, S. Amelinckx, TEM study of silicon on insulator structures obtained by oxygen ion implantation, *Micron Microsc. Acta* 18 (1987) 247–248.
- [20] A.N. Mikhaylov, D.I. Tetelbaum, V.A. Burdov, O.N. Gorshkov, A.I. Belov, D. A. Kambarov, V.A. Belyakov, V.K. Vasiliev, A.I. Kovalev, D.M. Gaponova, Effect of ion doping with donor and acceptor impurities on intensity and lifetime of photoluminescence from SiO<sub>2</sub> films with silicon quantum dots, *J. Nanosci. Nanotechnol.* 8 (2008) 780–788.
- [21] C. Ko, J. Joo, M. Han, B.Y. Park, J.H. Sok, K. Park, Annealing effects on the photoluminescence of amorphous silicon-nitride films, *J. Kor. Phys. Soc.* 48 (2006) 1277–1280.
- [22] T.V. Torchynska, L.G. Vega-Macotela, L. Khomenkova, A. Slaoui, Light-emitting mechanism varying in Si-rich-SiNx controlled by film's composition, *Adv. Nano Research* 5 (2017) 261–279.
- [23] J. Derr, K. Dunn, D. Riabinina, F. Martin, M. Chaker, F. Rosei, Quantum confinement regime in silicon nanocrystals, *Physica E* 41 (2009) 668–670.
- [24] M.L. Brongersma, P.G. Kik, A. Polman, K.S. Min, H.A. Atwater, Size-dependent electron-hole exchange interaction in Si nanocrystals, *Appl. Phys. Lett.* 76 (2000) 351–353.
- [25] C. Meier, A. Gondorf, S. Luttjohann, A. Lorke, H. Wiggers, Silicon nanoparticles: absorption, emission, and the nature of the electronic bandgap, *J. Appl. Phys.* 101 (2007) 103112–103118.
- [26] D.V. Tsu, G. Lucovsky, B.N. Davidson, Effects of the nearest neighbors and the alloy matrix on SiH stretching vibrations in the amorphous SiO<sub>x</sub>H (0<r<2) alloy system, *Phys. Rev. B* 40 (1989) 1795–1805.
- [27] W.J. Salcedo, F.J.R. Fernandez, E. Galeazzo, Structural characterization of photoluminescent porous silicon with FTIR spectroscopy, *Braz. J. Phys.* 27 (1997) 158–161.
- [28] M.V. Druenen, G. Collins, C. Glynn, C. O'Dwyer, J.D. Holmes, Functionalization of SiO<sub>2</sub> surfaces for Si monolayer doping with minimal carbon contamination, *ACS Appl. Mater. Interfaces* 10 (2018) 2191–2201.
- [29] A.G. Badou, T. Coradin, J. Maquet, F. Fröhlich, J. Livage, Spectroscopic characterization of biogenic silica, *J. Non-Cryst. Solids* 316 (2003) 331–337.
- [30] B. Parida, G. Lim, J. Choi, S. Palei, K. Kim, Hydrogen passivation effect on the conversion efficiency of Si solar cells by low-energy proton implantation, *Sol. Energy* 122 (2015) 486–496.
- [31] N.M. Johnson, D.K. Biegelsen, M.D. Moyer, Deuterium passivation of grain boundary dangling bonds in silicon thin films, *Appl. Phys. Lett.* 40 (1982) 882–884.
- [32] A. Slaoui, A. Barhdadi, J.C. Muller, P. Siffert, Passivation of laser-induced defects in silicon by low energy hydrogen ion implantation, *Appl. Phys. A* 39 (1986) 159–162.
- [33] S. Sivothaman, M. Rodot, J.C. Muller, B. Hartiti, M. Ghannam, H.E. Elgamel, J. Nijs, D. Sarti, Enhancement of diffusion length of pregettered multicrystalline silicon solar cells by hydrogen ion implantation at the end of the process, *Appl. Phys. Lett.* 62 (1993) 3172–3173.
- [34] W. Seifert, G. Morgenstern, M. Kittler, Influence of dislocation density on recombination at grain boundaries in multicrystalline silicon, *Semicond. Sci. Technol.* 8 (1993) 1687–1691.
- [35] P. Papakonstantinou, K. Somasundram, X. Cao, W.A. Nevin, Crystal surface defects and oxygen gettering in thermally oxidized bonded SOI wafers, *J. Electrochem. Soc.* 148 (2001) G36–G42.
- [36] O. Breitenstein, J. Bauer, T. Trupke, R.A. Bardos, On the detection of shunts in silicon solar cells by photo- and electroluminescence imaging, *Prog. Photovoltaics Res. Appl.* 16 (2008) 325–330.
- [37] D. Mankovics, A. Klossek, C. Krause, T. Arguirov, W. Seifert, M. Kittler, Luminescence of defects and breakdown sites in multicrystalline silicon solar cells, *Phys. Status Solidi* 209 (2012) 1908–1912.
- [38] D. Danilov, O. Vyvenko, A. Loshachenko, B. Ber, D. Kasantsev, N. Sobolev, Luminescent and electrical properties of oxygen-implanted silicon, *Phys. Status Solidi C* 14 (2017) 1700114–1700116.
- [39] B. Ünal, S.C. Bayliss, Electroluminescence and photovoltaic effects of anodically fabricated metal/porous Si/Si sandwich structures based on n-type ultravioletporous Si, *J. Appl. Phys.* 80 (1996) 3532–3539.
- [40] B. Sopori, Silicon solar-cell processing for minimizing the influence of impurities and defects, *J. Electron. Mater.* 31 (2002) 972–980.
- [41] M. Ichimura, H. Sakakibara, K. Wada, M. Karo, Efficiency of a solar cell with intermediate energy levels: an example study on hydrogen implanted Si solar cells, *J. Appl. Phys.* 114 (2013) 114505–114506.
- [42] M.A. Green, Accurate expressions for solar cell fill factors including series and shunt resistances, *Appl. Phys. Lett.* 108 (2016) 81111–81115.
- [43] A. Khanna, T. Mueller, R.A. Stangl, B. Hoex, P.K. Basu, A.G. Aberle, A fill factor loss analysis method for silicon wafer solar cells, *IEEE J. Photovolt.* 3 (2013) 1170–1177.